inorganics

MDPI

Article

SCAPS-1D Simulation for Device Optimization to Improve Efficiency in Lead-Free $CsSnI_3$ Perovskite Solar Cells

Hyun-Jae Park [1], Hyojung Son [2] and Byoung-Seong Jeong [1,2,*]

[1] Department of Hydrogen and Renewable Energy, Kyungpook National University, Daegu 41566, Republic of Korea
[2] KNU Advanced Material Research Institute, Kyungpook National University, Daegu 41566, Republic of Korea
* Correspondence: gatorever@knu.ac.kr

Abstract: In this study, a novel systematic analysis was conducted to explore the impact of various parameters, including acceptor density (N_A), individual layer thickness, defect density, interface defect density, and the metal electrode work function, on efficiency within the FTO/ZnO/$CsSnI_3$/NiO_x/Au perovskite solar cell structure through the SCAPS-1D (Solar Cell Capacitance Simulator in 1 Dimension) simulation. ZnO served as the electron transport layer (ETL), $CsSnI_3$ as the perovskite absorption layer (PAL), and NiO_x as the hole transport layer (HTL), all contributing to the optimization of device performance. To achieve the optimal power conversion efficiency (PCE), we determined the ideal PAL acceptor density (N_A) to be 2×10^{19} cm^{-3} and the optimal thicknesses to be 20 nm for the ETL (ZnO), 700 nm for the PAL ($CsSnI_3$), and 10 nm for the HTL (NiO_x), with the metal electrode remaining as Au. As a result of the optimization process, efficiency increased from 11.89% to 23.84%. These results are expected to contribute to the performance enhancement of eco-friendly, lead-free inorganic hybrid solar cells with Sn-based perovskite as the PAL.

Keywords: perovskite; photovoltaic solar cell; Pb-free; $CsSnI_3$; SCAPS

check for updates

Citation: Park, H.-J.; Son, H.; Jeong, B.-S. SCAPS-1D Simulation for Device Optimization to Improve Efficiency in Lead-Free $CsSnI_3$ Perovskite Solar Cells. *Inorganics* **2024**, *12*, 123. https://doi.org/10.3390/inorganics12040123

Academic Editor: Shuang Xiao

Received: 26 March 2024
Revised: 16 April 2024
Accepted: 19 April 2024
Published: 21 April 2024

1. Introduction

Because of environmental concerns and resource scarcity, it is considered difficult for energy production based on fossil fuels to be sustainable [1,2]. Solar energy has emerged as a promising alternative over the past few decades, offering a solution to these challenges [3,4]. In particular, perovskites, with their superior properties, have gained attention as a leading contender for next-generation solar cells [5,6]. The chemical formula of perovskite is ABX_3, where A comprises large cations (Cs^+, $NH_2CH_3NH_2^+$, $CH_3NH_3^+$), B comprises divalent cations (Pb^{2+}, Sn^{2+}), and X comprises monatomic halogen anions (I^-, Br^-, Cl^-) [7,8]. Due to their long diffusion lengths and high absorption coefficients (10^4 cm^{-1}), along with the benefits of flexibility, lightweight, and transparency, these materials hold economic advantages, spurring extensive research in the field [9–11].

PSCs have demonstrated rapid performance improvement, achieving efficiencies comparable to conventional solar cells, with a remarkable efficiency of 26.1% reported in 2023 [12]. Moreover, the parameters of the maximum theoretical limit (SQ-limit) employing the $CH_3NH_3PbI_{3-x}CL_x$ absorber (E_g~1.55 eV) have been reported as follows: current density (J_{SC}) is 27.20 mA/cm^2, open-circuit voltage (V_{OC}) is 1.28 V, fill factor (FF), and power conversion efficiency (PCE) is 90.2% and 31.4%, respectively [13,14]. This demonstrates the potential for the further advancement of perovskite solar cells, indicating a promising future.

However, several challenges remain unresolved for PSCs, including the development of commercially feasible next-generation perovskite materials and advancements in manufacturing technology [15,16]. Additionally, hybrid perovskites, such as methylammonium lead triiodide ($MAPbI_3$) and formamidinium lead triiodide ($FAPbI_3$), which have been

extensively studied, exhibit poor stability against heat and moisture [17,18]. As a result, the fabrication of hybrid PSCs requires careful environmental control, such as glove boxes or drying chambers [19,20]. Currently, due to these drawbacks of organic-based perovskites, there is an increasing amount of research being conducted on photovoltaic solar cells that utilize inorganic perovskites [21–23].

Therefore, in this study, we selected an inorganic perovskite material to fabricate an all-inorganic PSC. Among them, one of the primary concerns in all-inorganic perovskites is the use of lead (Pb) in the PAL of most high-efficiency photovoltaic cells (PVs) [24–26]. Lead-based perovskites produce harmful by-products like PbI_2 when decomposed, which can cause oxidative stress when exposed to the human body, potentially harming the nervous, reproductive, blood, and kidney systems [27,28]. As an alternative to solving these issues, research into tin-based (Sn-based) perovskites has emerged as a new area of focus [29]. This tin-based inorganic perovskite ($CsSnX_3$) provides benefits such as a bandgap close to 1.4 eV, high mobility, and a high absorption coefficient (greater than 10^5 cm^{-1}) [30,31].

In particular, $CsSnI_3$ has a bandgap of 1.3–1.4 eV and exhibits a high absorption coefficient of 10^4 cm^{-1} in the visible range [32]. Additionally, its low exciton binding energy (10–20 meV) facilitates easier carrier separation compared to typical organic absorbers [33]. In addition, it has the advantage of superior thermal stability with a melting point of 451 °C, which is higher than that of conventional perovskites such as $MASnI_3$ and $FASnI_3$, which have a melting point of 200 °C [34]. Because of these characteristics, $CsSnI_3$ has demonstrated the highest experimental efficiency of 10.1% among reported Pb-free Sn-based perovskite materials [35].

As for ZnO, used as the electron transport layer (ETL) material, it is environmentally friendly and exhibits high carrier mobility [36]. With a wide bandgap (3.3 eV) and a significant exciton binding energy, ZnO is being studied as one of the most interesting ETL materials [37,38]. Especially for ZnO single nanowires, they feature electron mobility of up to ~1000 $cm^2/V{\cdot}s$ and can be doped with both n-type and p-type materials [39].

Regarding NiO_x, which serves as the hole transport layer (HTL) material, it exhibits a large bandgap (>3.5 eV) with superior transparency in the visible range [40]. This characteristic can minimize losses such as charge recombination, enhance charge transport, and provide optimal energy-level alignment with various photoactive absorbers due to its sufficient conductivity and chemical stability [38,41].

Based on these properties, we selected $CsSnI_3$ as PAL, ZnO as ETL, NiO_x as HTL and constructed an environmentally friendly Sn-based Pb-free PSC device (FTO/ZnO/$CsSnI_3$/NiO_x/Au). However, there are few studies systematically analyzing the influence of each parameter (such as acceptor density, layer thickness, interface defect density, and metal electrode work function) in the FTO/ZnO/$CsSnI_3$/NiO_x/Au structure [42].

Therefore, in this study, based on the consideration of each parameter, we systematically analyzed the effect of key parameters, such as acceptor density, layer thickness, defect density, interfacial defect density, and metal electrode work function, on the performance of photovoltaic solar cells and proposed an optimized solar cell structure, FTO/ZnO/$CsSnI_3$/NiO_x/Au, which is a completely inorganic device architecture.

Of course, practically, in the experimental phase, controlling interface defects is crucial due to their significant impact on device performance. Such defects can arise from material inhomogeneity, varying process conditions, and the nature of surface treatments [43,44]. Notably, material inhomogeneity, particularly the intrinsic surface defects of zinc oxide, can lead to severe carrier recombination, as highlighted in reference [45]. Therefore, for the scope of this simulation research, we are concentrating on the alteration of specific parameters—the density of interface defects and overall defect density—to determine their impact on the power conversion efficiency (PCE) of the device. These parameters need to be closely studied and adjusted as necessary before we proceed with full-scale practical experiments.

2. Results and Discussion

2.1. Simulation under Initial Conditions

The device performance was analyzed based on key parameters such as open-circuit voltage (V_{OC}), short-circuit current density (J_{SC}), fill factor (FF), and power conversion efficiency (PCE). Importantly, the FF was calculated using Equation (1), as reported in references [46,47].

$$FF = \frac{J_{max}V_{max}}{J_{SC}V_{OC}} \quad (1)$$

The parameter for power conversion efficiency (PCE) was determined by the following in Equation (2):

$$PCE = \frac{I_{SC} \cdot V_{OC} \cdot FF}{P_{in}} \quad (2)$$

where I_{SC} is the short-circuit photocurrent, and P_{in} is the input power. The quantum efficiency (QE) is the ratio of the number of charge carriers collected by the solar cell to the number of incident photons at a specific energy, which is calculated as follows in Equation (3) [48].

$$QE(\%) = \frac{\text{number of reacted electrons}}{\text{number of incident photons}} \times 100\% \quad (3)$$

The initial simulation results for the current density–voltage (J–V) plot and the quantum efficiency (QE) curve for FTO/ZnO/$CsSnI_3$/NiO_x/Au PSC are depicted in Figure 1a,b, respectively. The parameters for the current density–voltage (J–V) characteristics, including V_{OC}, J_{SC}, FF, and PCE, were 1.01 V, 15.55 mA/cm^2, 75.78%, and 11.89%, respectively. The initial efficiency obtained was low at 11.89%, and accordingly, the levels of parameters were adjusted to investigate the effects of V_{OC}, J_{SC}, and FF on PCE for the optimization of this perovskite solar cell device.

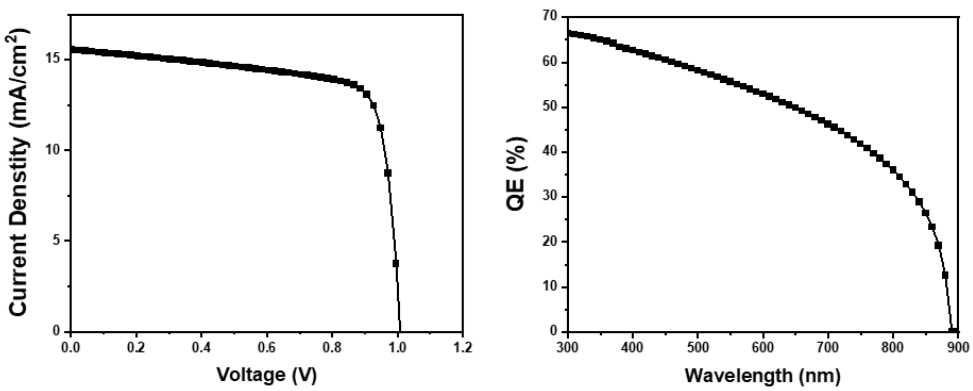

(**a**) (**b**)

Figure 1. (**a**) Simulated initial J–V curve of PSC cell; (**b**) simulated initial QE curve of PSC cell.

2.2. Efficiency Variation Depending on Acceptor Density (N_A) of PAL

Figure 2 illustrates the variation in V_{OC}, J_{SC}, FF, and PCE with PAL acceptor density (N_A) within the range of 2×10^{19} to 10^{21} cm^{-3}. The initial setting value was 1×10^{20} cm^{-3}, referenced to the optimal value determined in a prior study, while 2×10^{19} cm^{-3} represents the minimum N_A providing a certain PV response [49,50]. The PCE exhibited an overall decreasing trend as N_A increased, with a PCE of 22.05% when N_A was 2×10^{19} cm^{-3}, in contrast to a PCE of 0.53% when N_A was 1×10^{21} cm^{-3}, indicating the significant impact of N_A on PCE. J_{SC} and FF exhibited similar trends to PCE, while V_{OC} increased up to 7×10^{19} cm^{-3} before decreasing. This increase in V_{OC} is attributed to the fermi level (E_f) approaching the valence band (VB) due to increased acceptor doping [51]. Subsequently, the increase in charge carriers led to a decrease in V_{OC}. Two predominant factors contributed

to the efficiency decrement with increasing N_A; firstly, this included the increase in sheet resistance [52,53]. With the increase in doping density, the sheet resistance of PAL for N_A in p-type perovskite materials increases, impeding hole mobility to HTL, accelerating the recombination of photo-generated carriers, decreasing the generation of electron-hole pairs, and resulting in a decrease in efficiency owing to a reduction in the minority carrier concentration, mobility, and diffusion length. Equation (4) describes the decrement in saturation current (I_O) with increasing N_A [54].

$$I_O = Aqn^2{}_i\left(\frac{D_e}{L_eN_A} + \frac{D_h}{L_hN_D}\right) \tag{4}$$

where I_O is the saturation current, n_i is the intrinsic concentration, A is the diode quality factor, q is the elementary charge, N_A and N_D are the acceptor and donor charge concentrations, L_e and L_h are the electron and hole diffusion length, and D_e and D_h are diffusion coefficient, respectively.

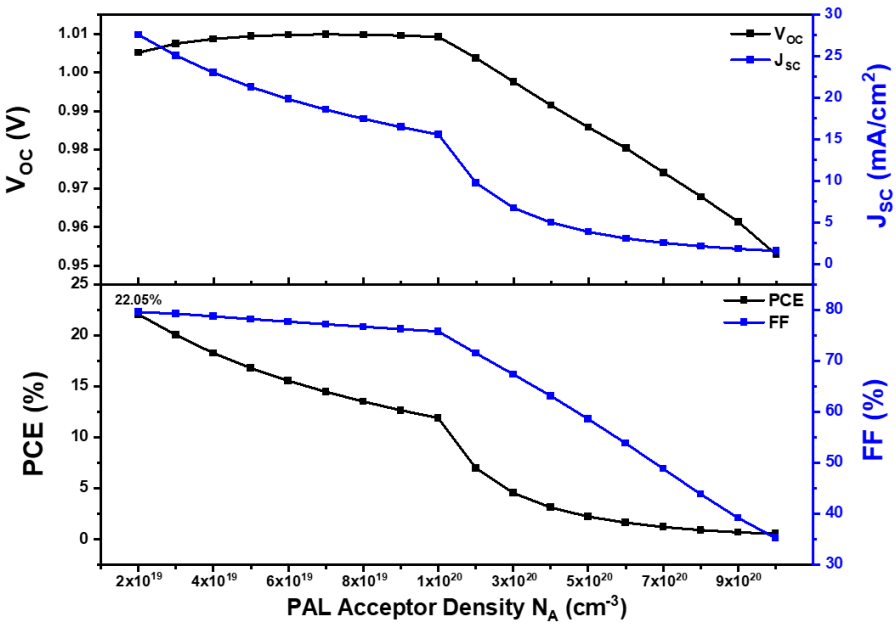

Figure 2. The variation in V_{OC}, J_{SC}, FF, and PCE with the acceptor density (N_A)of PAL.

The secondary causative factor is the incidence of Auger recombination due to high doping concentrations [55,56]. In devices where the concentration exceeds 10^{18} cm^{-3}, dopants trigger Auger recombination, ultimately leading to a reduction in the performance parameters of the photovoltaic device.

Consequently, by setting the optimal N_A value of 2×10^{19} cm^{-3} for the PAL, J_{SC}, and PCE achieved a notable enhancement from 15.55 mA/cm^2 to 27.58 mA/cm^2 and from 11.89% to 22.05%, respectively. The other parameters were maintained consistent with previous settings. According to a previously published paper, the optimal N_A value of 2×10^{19} cm^{-3} aligns with $CsSnI_3$, typically exhibiting a maximum p-type doping concentration of 10^{19} to 10^{20} cm^{-3} even in the undoped case at room temperature, and the addition of Sn can increase the N_A value [57]. This occurrence is ascribed to the presence of hydrogen anions in Sn-rich environments, facilitating a shift in the Fermi level (E_f) towards the valence band maximum (VBM) and considerably increasing the doped hole concentration [58]. The N_A value of 2×10^{19} cm^{-3} selected in this study aligns with the optimal values previously reported at 10^{19} and 7×10^{19} cm^{-3} [59,60].

2.3. Optimization of Each Layer's Thickness

Each layer of the PSC serves a distinctive role in the performance of the cell, so it is important to adjust the thickness of each layer for optimal cell performance. The optimization of layer thickness was executed by preserving the uniform thickness for two layers and varying the thickness of the residual layers.

2.3.1. Optimization of ZnO Thickness

ZnO is employed as an electron transport layer (ETL) material in the n-i-p structure as the initial substance to be exposed to incoming light. For the initial device fabrication, optimizing the thickness of ZnO is important. Thus, referencing the 16 nm and 20 nm ZnO coating thicknesses fabricated using spin-coating in papers [61,62], our study conducted optimization within the range of 10 to 500 nm for ZnO coating. The graph in Figure 3 describes the impact of ZnO thickness on V_{OC}, J_{SC}, FF, and PCE. As the thickness of ZnO increased from 10 nm to 20 nm, PCE increased from 22.05% to 22.32%. The low PCE at a ZnO thickness of 10 nm can be attributed to insufficient layer thickness for effective electron extraction and transport, leading to inefficiencies in charge collection, resulting in lower FF and PCE [63,64]. In the thickness range of 20 nm to 50 nm, the FF value exhibited an overall decrease followed by an increase thereafter. This phenomenon was ascribed to the relatively small decrease in J_{SC} compared to V_{OC} at this thickness. Similar observations were reported in a previous study [65]. Furthermore, the decrease in PCE with increasing thickness is associated with the acceleration of electron-hole pair recombination due to the surface roughness with thicker layers [66]. This precipitates an increase in series resistance, causing a reduction in J_{SC} and V_{OC}. Therefore, we derived the conclusion that a thinner ETL thickness leads to an increase in efficiency. Based on this conclusion, we set the optimal thickness to 20 nm.

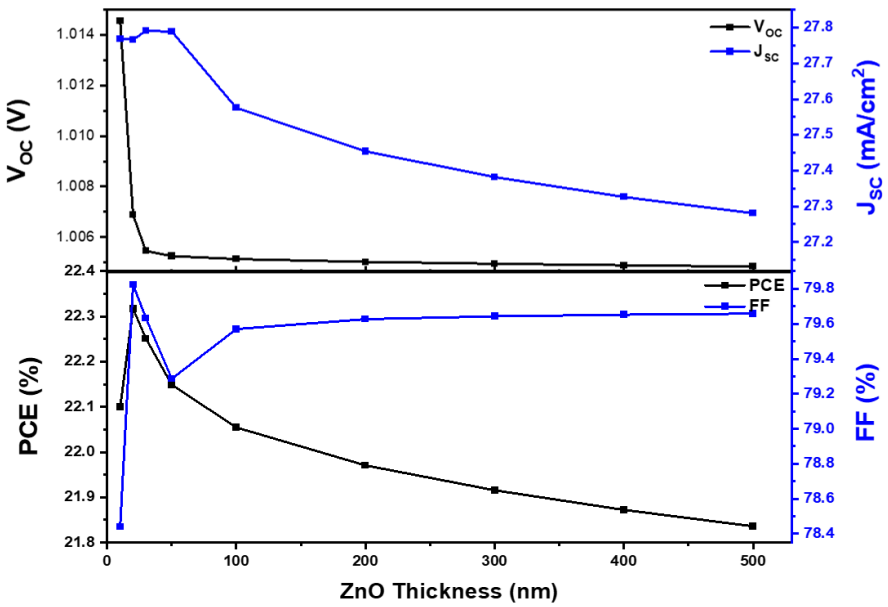

Figure 3. The variation in V_{OC}, J_{SC}, FF, and PCE with ZnO thickness.

2.3.2. Optimization of PAL Thickness

Upon light incidence on the absorption stratum of a solar cell, electron-hole pairs are generated. For effective operation of the solar cell, it is important that these pairs reach each electrode without recombination [67]. To achieve this, optimizing the thickness of the perovskite absorption layer (PAL) is essential. When the PAL thickness is excessively thick, it increases the time required for the absorption and conversion of light energy, leading to recombination [68]. Conversely, an excessively thinner PAL can impede light absorption, decreasing the current density [69]. To find the optimum thickness, optimization was

performed in the range of 100 to 1200 nm. The graph in Figure 4 illustrates the influence of PAL thickness on V_{OC}, J_{SC}, FF, and PCE. V_{OC}, J_{SC}, and PCE predominantly exhibited an overall increasing trend, while FF increased in the range of 100 to 200 nm and then decreased from 200 to 1200 nm. The initial increase in FF was attributed to the efficient charge transport with increasing thickness, while the subsequent decrease was due to a reduction in shunt resistance and an increase in series resistance [70]. Furthermore, PCE increased in the range of 100 to 700 nm, reaching its highest efficiency of 22.64% at a thickness of 700 nm. This was due to the substantial photon absorption by PAL, resulting in the generation of the most electron-hole pairs [71]. However, from 700 to 1200 nm, PCE decreased due to the resistance caused by recombination [72,73].

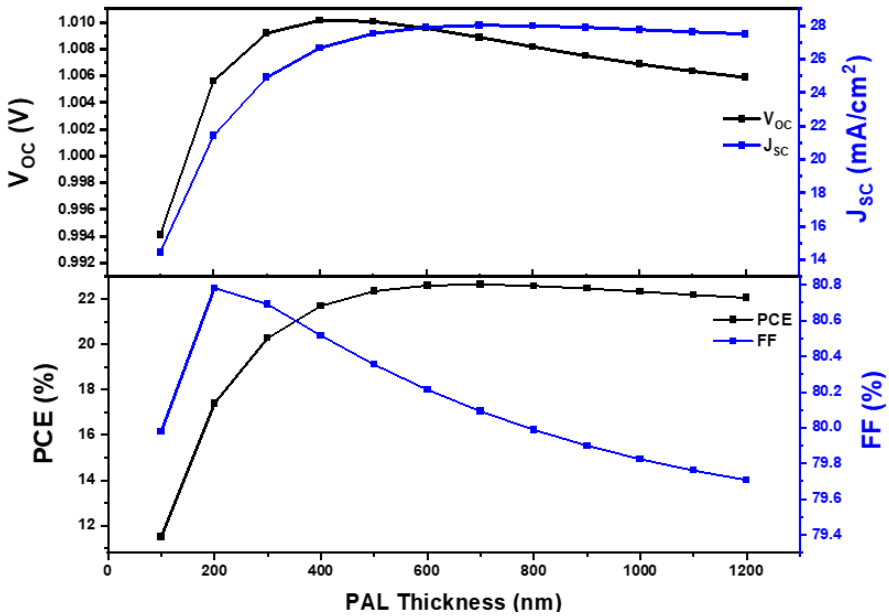

Figure 4. The variation in V_{OC}, J_{SC}, FF, and PCE with PAL thickness.

Equation (5) depicts the mathematical relation between the thickness and absolute absorption rate of the absorber [74]. By employing this equation, the absolute absorption rate of the absorber can be computed, facilitating the determination of the optimal thickness of PAL.

$$R_{absorber} = \frac{pt}{A^2} \tag{5}$$

Here, $R_{absorber}$ is the absorber resistance, p is the resistance of the PAL, t is the thickness of PAL, and A is the cross-sectional area. This results in Equation (5); as the PAL thickness increases, the absorber resistance rises. This phenomenon generally leads to an increase in V_{OC}, J_{SC}, and FF values. However, the increase in absorber thickness also enhances the photon energy absorption rate [75]. Considering these electrical and optical property changes, an optimal PCE at 22.64% was achieved when the absorber thickness was 700 nm.

2.3.3. Optimization of NiO_x Thickness

The hole transport layer (HTL) serves a crucial role in enhancing the transport of charge carriers (holes) and prevents direct contact between the PAL and anode through capping [76,77]. Figure 5a illustrates the influence of NiO_x thickness within the range of 10 to 500 nm on V_{OC}, J_{SC}, FF, and PCE. The peak efficiency of 22.76% was achieved at the smallest thickness of 10 nm, while PCE decreased as the thickness increased, reaching its lowest efficiency of 19.1% at the maximum thickness of 500 nm. This result was primarily attributed to the increase in HTL thickness, causing an increase in the series resistance of the solar cell [78]. Consequently, it became challenging for holes to reach the anode, resulting in recombination and causing a decrease in V_{OC}, J_{SC}, FF, and overall PCE.

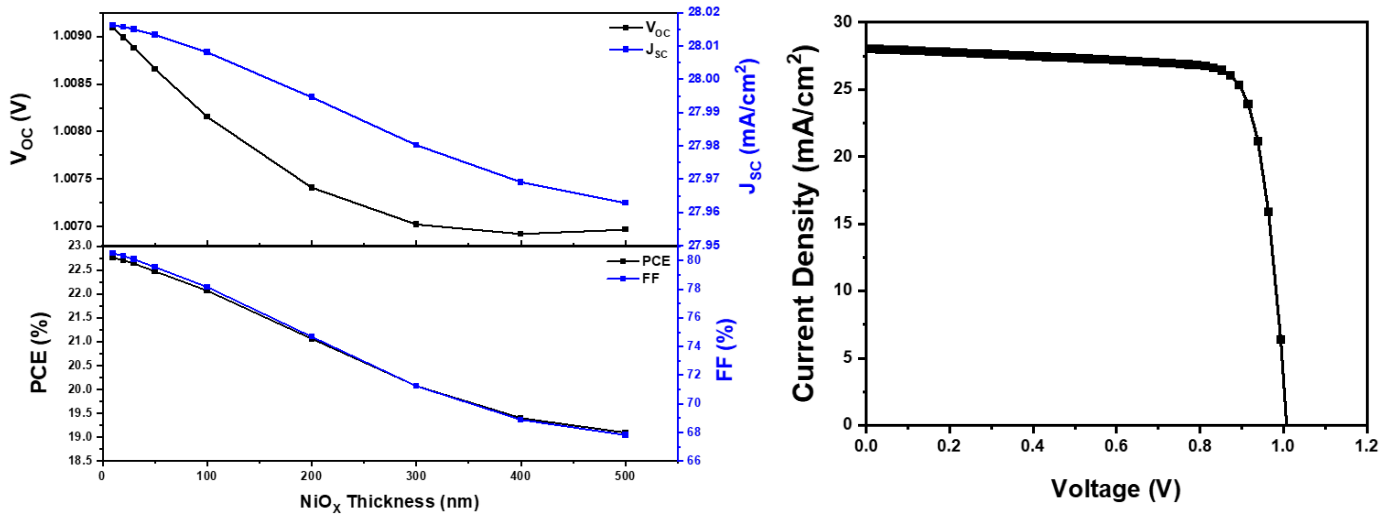

(**a**) (**b**)

Figure 5. (**a**) V_{OC}, J_{SC}, FF, and PCE with NiO_x thickness; (**b**) current density–voltage (J–V) curve of PSC cell with thickness optimization: ZnO (20 nm), $CsSnI_3$ (700 nm), and NiO_x (10 nm).

Following NiO_x thickness optimization, the optimal thickness for ZnO and $CsSnI_3$ were determined to be 20 nm and 700 nm, respectively. As shown in Figure 5b, the corresponding values for V_{OC}, J_{SC}, FF, and PCE were 1.01 V, 28.02 mA/cm^2, 80.5%, and 22.76%, respectively. The PCE graphs based on the thickness of each layer demonstrated that the thickness of each layer had a substantial impact on the performance of the PSC.

2.4. Optimization of PAL Defect Density and Interface Defect Density

The defect density typically increases the recombination of photogenerated carriers at both the bulk material and interface defects, leading to an increase in the quasi-saturation current density (J_0) and consequently reducing both J_{SC} and V_{OC} [79,80]. Therefore, to investigate the effect of defect density on Jsc, Voc, FF, and PCE, simulations were conducted for the defect density of the PAL. Figure 6a demonstrates the influence of the PAL defect density varying from 10^{11} to 10^{18} cm^{-3} on V_{OC}, J_{SC}, FF, and PCE.

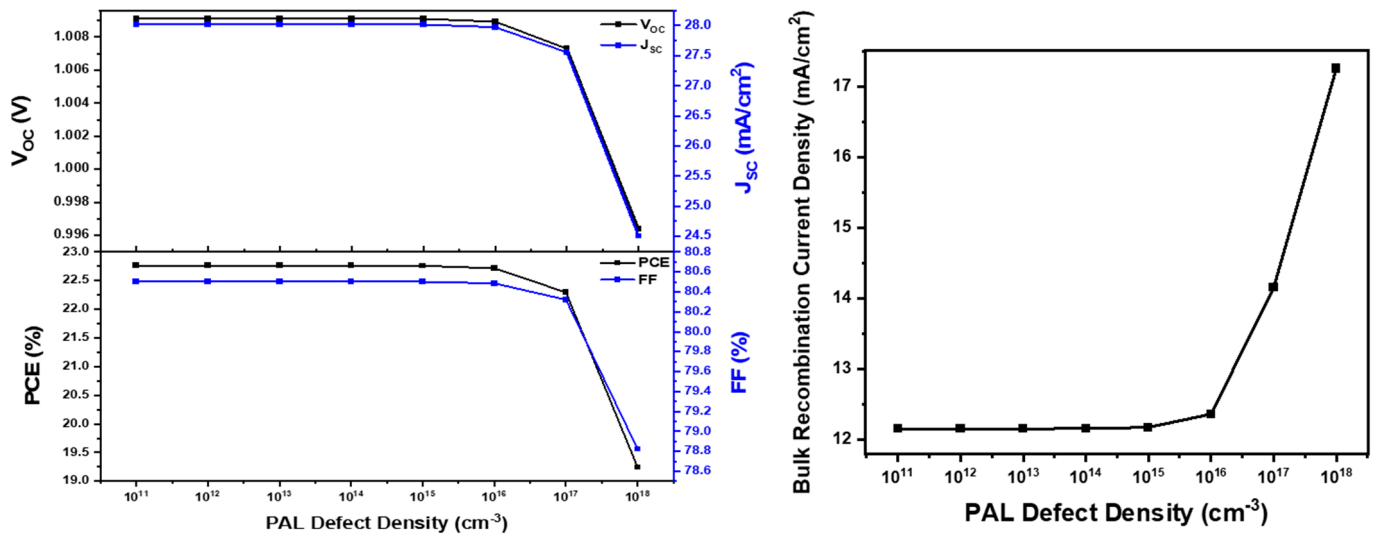

(**a**) (**b**)

Figure 6. (**a**) The variation in V_{OC}, J_{SC}, FF, and PCE with PAL defect density; (**b**) the variation in bulk recombination current density with PAL defect density.

The efficiency remained stable within the initial defect density range of 10^{11}~10^{15} cm^{-3}; however, a sharp decrease in efficiency was observed from 10^{16} cm^{-3} onwards. This phenomenon can be attributed to the increase in defect density, which leads to an increase in recombination current and accelerated carrier recombination [81].

As described in Figure 6b, the graph of bulk recombination current density caused by the PAL defect density confirmed the increase in the recombination current at a defect density of 10^{16} cm^{-3}. Ultimately, the lowest efficiency of 19.24% was observed at the maximum value of 10^{18} cm^{-3}. This was attributed to a degradation in film quality due to the surge in defect density, leading to an accelerated recombination rate and shortened carrier lifetime, and consequently leading to decreased efficiency [82,83]. Based on these results, the optimal defect density was adjusted to the conventional value of 10^{14} cm^{-3}, thereby maintaining the original efficiency of 22.76%. These results also exhibited a similar tendency as those reported in previously conducted research [84,85].

The performance of the device significantly varies depending on the defect density of the interface layer, as shown in Figure 7a,b. Figure 7a,b illustrate the impact of defect density on V_{OC}, J_{SC}, FF, and PCE for the ZnO/PAL interface and PAL/NiO_x interface, respectively, in the range of 10^8 to 10^{20} cm^{-3}.

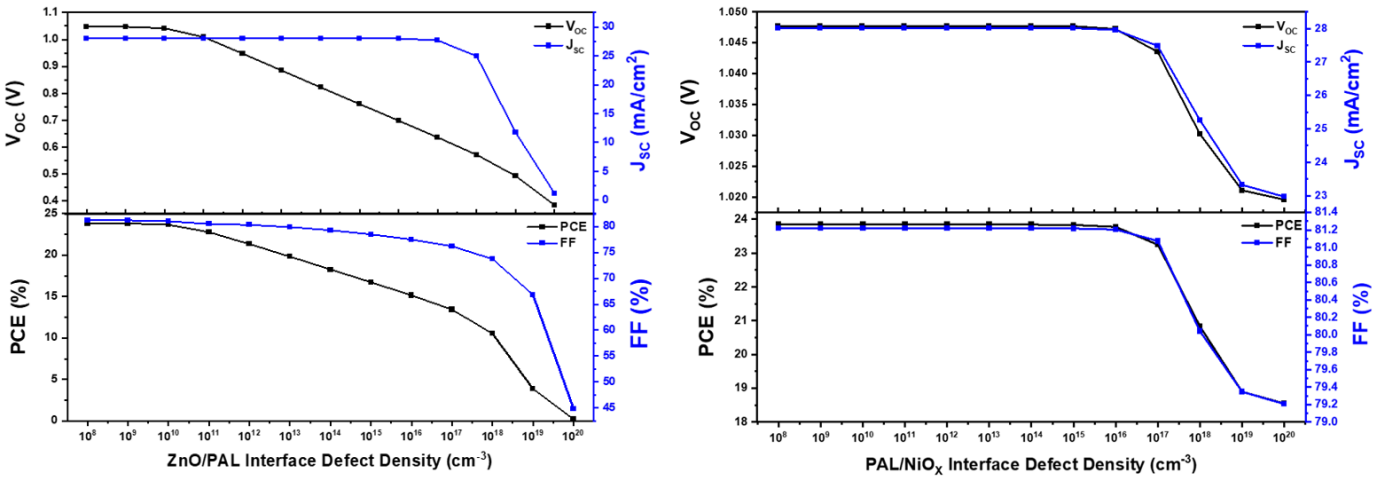

(**a**) (**b**)

Figure 7. (**a**) The variation in PCE with ZnO/PAL interface defect density; (**b**) the variation in PCE with PAL/NiO_x interface defect density.

As the defect density increases at both interfaces, the PCE initially remains stable without significant changes. However, for the ZnO/PAL interface, the PCE begins to gradually decrease, starting from 10^{11} cm^{-3} in Figure 7a. In contrast, in the case of the PAL/NiO_x interface, efficiency remained within the range of 10^8 to 10^{15} cm^{-3}, but it began to decrease sharply, starting from 10^{16} cm^{-3} in Figure 7b. This decrease in efficiency is attributed to defects acting as recombination centers, leading to a reduction in charge carrier density as the defect density increases [86]. The sharp decrease at a certain interface defect density is attributed to a rapid decline in photon absorption when exceeding a specific N_t value at each interface [87]. As a result, PCE was enhanced from 22.76% to 23.84% by setting the optimal interface defect density for both interfaces at 10^8 cm^{-3}.

2.5. Optimization of Metal Electrode Work Function

For the design of high-performing solar cells, the choice of suitable electrodes is critical. For this part, experiments were carried out using metal electrode materials such as Al (4.2 eV), Cu (4.6 eV), Ag (4.7 eV), Fe (4.8 eV), and Au (5.1 eV) [88]. Figure 8 illustrates the influence of metal electrode work functions on V_{OC}, J_{SC}, FF, and PCE. As the work function increased, all parameters exhibited a tendency to increase proportionally. As a result, PCE was lowest at 4.17% for Al, which had the lowest work function of 4.2 eV, while Au, with

the highest work function of 5.1 eV, achieved an optimal efficiency of 23.84%. A reason for the decrease in efficiency as the work function of the metal electrodes decreased was due to the increased Schottky barrier impeding hole transport, leading to a decrease in FF [89]. Furthermore, regarding higher work functions mentioned in Ref. [90], such as W (5.22 eV), Ni (5.5 eV), Pt (5.7 eV), Se (5.9 eV), PCE shows saturated behavior indicating the absence of additional chemical interactions between the PAL and these metals (W, Ni, Pt, Se). Based on these results, this study utilized Au as the optimal metal electrode. These findings concur with various simulation results [91,92].

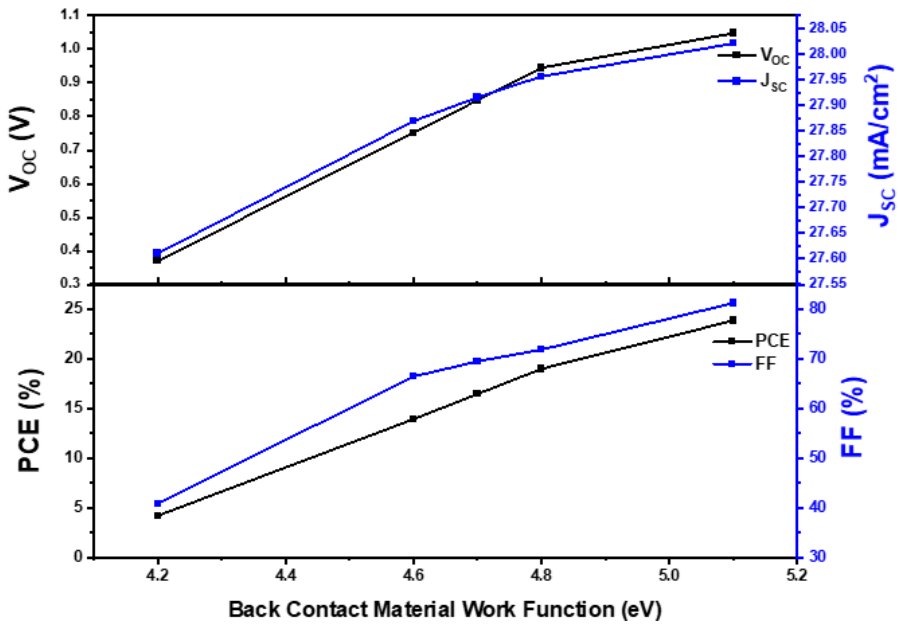

Figure 8. The variation in V_{OC}, J_{SC}, FF, and PCE with back contact material work function.

3. Materials and Methods

3.1. Numerical Modeling

The numerical simulations performed in this study were based on the SCAPS-1D (Solar Cell Capacitance Simulation in 1 Dimension) (ver. 3.3.11) simulator. This computational tool, developed by Dr. M. Burgelman of the University of Gent in Belgium, enables the design and simulation of up to seven heterojunction layers [93]. The simulations were based on Poisson's Equation (6) and the continuity Equations (7) and (8) for each electron and hole, respectively [94,95].

$$\frac{d}{dx}\left(-\varepsilon(x)\frac{d\psi}{dx}\right) = q\left[p(x) - n(x) + N^{+}{}_{d}(x) - N^{-}{}_{a}(x) + p_t(x) - n_t(x)\right] \quad (6)$$

$$\frac{dp_n}{dt} = G_p - \frac{P_n - P_{n0}}{\tau_p} - P_n\mu_p\frac{dE}{dx} - \mu_p E\frac{dp_n}{dx} + D_p\frac{d^2p_n}{dx^2} \quad (7)$$

$$\frac{dn_p}{dt} = G_n - \frac{n_p - n_{p0}}{\tau_n} + n_p\mu_n\frac{dE}{dx} + \mu_n E\frac{dn_p}{dx} + D_n\frac{d^2n_p}{dx^2} \quad (8)$$

In this equation, ε is the dielectric constant, q is the charge of an electron, G is the generation rate, D is the diffusion coefficient, ψ is the electrostatic potential, E is the electric field, and $p(x)$, $n(x)$, $p_t(x)$, and $n_t(x)$ are free holes, free electrons, trapped holes, and trapped electrons, respectively. $N^{+}{}_{d}$ refers to doping concentration-like ionized donors, $N^{-}{}_{a}$ represents doping concentration-like ionized acceptors, and x is the direction along the thickness. In this study, following the standard test conditions (STC), the spectrum used in all simulations was the AM1.5G spectrum, the incident light power was set at 1000 W/m^2, the operating point voltage set to 0 V, and the temperature was set at 300 K [96].

3.2. Device Structure

Figure 9a illustrates a solid-state planar heterojunction p-i-n structure device composed of FTO/ZnO/$CsSnI_3$/NiO_x/Au. In this device, the perovskite material ($CsSnI_3$) is sandwiched between the n-type hole transport layer (HTL) NiO_x and the p-type electron transport layer (ETL) ZnO, with Au serving as the metal electrode. Figure 9b presents a simplified flat band energy diagram of the PSC. The work functions of FTO and Au are 4.4 eV and 5.1 eV, respectively [97,98]. The highest occupied molecular orbital (HOMO) and lowest unoccupied molecular orbital (LUMO) levels for ZnO, $CsSnI_3$, and NiO_x were 4.0 eV and 7.3 eV, 3.6 eV and 5.0 eV, and 1.8 eV and 5.4 eV, respectively [99–101]. Upon light irradiation, weakly bounded excitons were generated in the PAL of this device. These excitons undergo a dissociation process, rapidly separating into electrons and holes prior to recombination, promoting effective carrier transport within the device [102]. The energy structure depicted in the band diagram in Figure 9b facilitates the efficient movement of electrons and holes in the conduction and valence bands, respectively, significantly influencing the overall performance of the device.

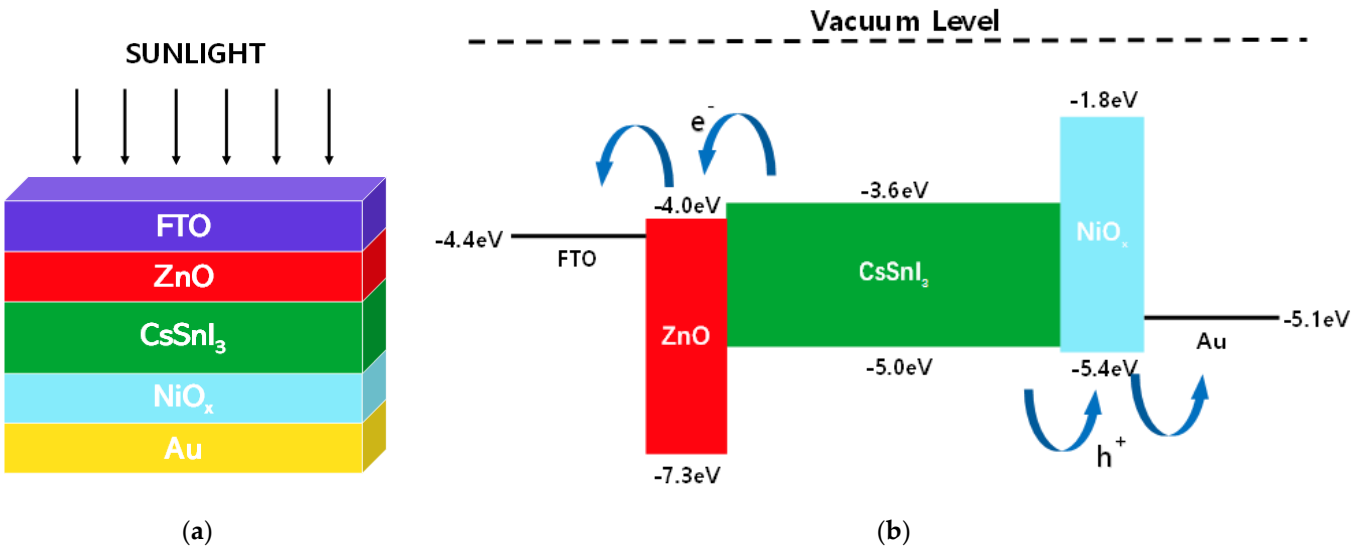

Figure 9. (**a**) The basic schematic diagram of the FTO/ZnO/$CsSnI_3$/NiO_x/Au perovskite solar cell device structure; (**b**) the energy band diagram of the PSC layers.

Table 1 presents the initial parameters of each material used in the FTO/ZnO/$CsSnI_3$/NiO_x/Au PSC simulations. The initial thicknesses of FTO, ZnO, $CsSnI_3$, and NiO_x were 500 nm, 100 nm, 1000 nm, and 30 nm, respectively [103–105]. The bandgap and electron affinity for each material are given as follows: FTO (3.2 eV, 4.4 eV), ZnO (3.3 eV, 4.0 eV), $CsSnI_3$ (1.4 eV, 3.6 eV), and NiO_x (3.6 eV, 1.8 eV) [106–109]. For the perovskite absorption layer (PAL), the band-to-band recombination model was maintained at a radiative recombination coefficient of 3×10^{-11} cm^3 and an Auger capture rate of 1×10^{-29} cm^6/s for both carriers (electrons and holes) [110,111]. The dielectric permittivity values for each material were 9, 8.656, 9.93, and 10.7, respectively. The thermal velocity of charge carriers (electrons and holes) in all layers was maintained at 10^7 cm/s. For interfacial layers, the defect type was set as neutral, with a Gaussian energy distribution, and the reference energy level for defect (E_t) was set above E_V. The capture cross-section for both types of charge carriers (electrons and holes) was 10^{-19} cm^{-3}, and the total charge carrier density was set at 1.0×10^{11} cm^{-3}. The variations in the parameters are listed in Table 2. Additionally, the band-to-band recombination model was maintained at zero for FTO, ETL, and HTL layers. Furthermore, the tunneling effect was not considered in the simulation.

Table 1. The initial parameters of each material used in the FTO/ZnO/$CsSnI_3$/NiO_x/Au PSC simulations.

Parameter	FTO [106]	ZnO [107]	$CsSnI_3$ [108]	NiO_x [109]
Thickness (nm)	500	100	1000	30
Bandgap (eV)	3.2	3.3	1.4	3.6
Electron affinity (eV)	4.4	4.0	3.6	1.8
Dielectric permittivity (relative)	9	8.656	9.93	10.7
CB effective density of states (cm^{-3})	2.2×10^{18}	2.2×10^{18}	1.0×10^{18}	2.8×10^{19}
VB effective density of states (cm^{-3})	1.8×10^{19}	1.8×10^{19}	1.0×10^{19}	1.8×10^{19}
Electron thermal velocity (cm/s)	1.0×10^{7}	1.0×10^{7}	1.0×10^{7}	1.0×10^{7}
Hole thermal velocity (cm/s)	1.0×10^{7}	1.0×10^{7}	1.0×10^{7}	1.0×10^{7}
Electron mobility (cm^2/Vs)	20	100	1500	12
Hole mobility (cm^2/Vs)	10	25	585	2.8
Shallow uniform donor density N_D (cm^{-3})	1.0×10^{18}	1.0×10^{18}	-	-
Shallow uniform acceptor density N_A (cm^{-3})	-	-	1.0×10^{20}	1.0×10^{15}
Defect density N_t (cm^{-3})	1.0×10^{15}	1.0×10^{15}	1.0×10^{15}	1.0×10^{15}

Table 2. The initial parameters of interfacial layers.

Parameter	ETL/PAL	PAL/HTL
Defect density	Neutral	Neutral
Capture cross-section for electrons (cm^{-3})	10^{-19}	10^{-19}
Capture cross-section for holes (cm^{-3})	10^{-19}	10^{-19}
Reference for the defect energy level E_t	E_V	E_V
Energetic distribution	Gaussian	Gaussian
Total density (cm^{-3})	1.0×10^{11}	1.0×10^{11}

4. Conclusions

In this study, in the device structure of FTO/ZnO/$CsSnI_3$/NiO_x/Au, various parameters, including the acceptor density (N_A) of the perovskite absorber layer (PAL), the thickness of each material layer, the defect density of PAL, the interface defect density, and work function of the metal electrode, were optimized. The parameters were optimized such that the N_A of the PAL was 2×10^{19} cm^{-3}, the thicknesses of the ETL (ZnO), PAL ($CsSnI_3$), and HTL (NiO_x) were 20 nm, 700 nm, and 10 nm, respectively, the PAL defect density was 10^{14} cm^{-3}, and interface defect density for ZnO/PAL and PAL/NiO_x was 10^8 cm^{-3}. As a result, the performance of the device was enhanced, with V_{OC}, J_{SC}, FF, and PCE improving from 1.01 to 1.05 V, 15.55 to 28.02 mA/cm^2, 75.78 to 81.22%, and 11.89 to 23.84%, respectively. This emphasizes the potential for the high-efficiency design of environmentally friendly, lead-free perovskite solar cells based on $CsSnI_3$.

Author Contributions: Conceptualization, H.-J.P. and B.-S.J.; software, H.-J.P. and H.S.; methodology, H.-J.P. and B.-S.J.; formal analysis, H.-J.P., H.S. and B.-S.J.; writing—original draft preparation, H.-J.P.; writing—review and editing, B.-S.J.; supervision, B.-S.J. All authors have read and agreed to the published version of the manuscript.

Funding: This work was supported by the Industrial Technology Innovation Program funded by the Ministry of Trade, Industry & Energy (MOTIE, Korea) [No. 20015778].

Data Availability Statement: The data presented in this study are available upon request from the corresponding author.

Conflicts of Interest: The authors declare no conflicts of interest.

References

1. Yao, L. New energy utilization in environmental design and realization. *Energy Rep.* **2022**, *8*, 9211–9220. [CrossRef]
2. Nunes, F.C.; de Jesus Alves, L.; Bitterncourt, P.; Prasad, M.N.V. Nonfossil energy targets for environmental sustainability. In *Decarbonization Strategies and Drivers to Achieve Carbon Neutrality for Sustainability*; Elsevier: Amsterdam, The Netherlands, 2024; pp. 27–44.
3. Ashraf, M.; Ayaz, M.; Khan, M.; Adil, S.F.; Farooq, W.; Ullah, N.; Nawaz Tahir, M. Recent trends in sustainable solar energy conversion technologies: Mechanisms, prospects, and challenges. *Energy Fuels* **2023**, *37*, 6283–6301. [CrossRef]
4. Hassan, Q.; Viktor, P.; Al-Musawi, T.J.; Ali, B.M.; Algburi, S.; Alzoubi, H.M.; Al-Jiboory, A.K.; Sameen, A.Z.; Salman, H.M.; Jaszczur, M. The renewable energy role in the global energy Transformations. *Renew. Energy Focus* **2024**, *48*, 100545. [CrossRef]
5. Nie, T.; Fang, Z.; Ren, X.; Duan, Y.; Liu, S. Recent advances in wide-bandgap organic–inorganic halide perovskite solar cells and tandem application. *Nano Micro Lett.* **2023**, *15*, 70. [CrossRef] [PubMed]
6. Bati, A.S.; Zhong, Y.L.; Burn, P.L.; Nazeeruddin, M.K.; Shaw, P.E.; Batmunkh, M. Next-generation applications for integrated perovskite solar cells. *Commun. Mater.* **2023**, *4*, 2. [CrossRef]
7. Qian, J.; Xu, B.; Tian, W. A comprehensive theoretical study of halide perovskites ABX_3. *Org. Electron.* **2016**, *37*, 61–73. [CrossRef]
8. Shaw, B.K.; Castillo-Blas, C.; Thorne, M.F.; Gómez, M.L.R.; Forrest, T.; Lopez, M.D.; Chater, P.A.; McHugh, L.N.; Keen, D.A.; Bennett, T.D. Principles of melting in hybrid organic–inorganic perovskite and polymorphic ABX_3 structures. *Chem. Sci. J.* **2022**, *13*, 2033–2042. [CrossRef]
9. Jung, H.S.; Han, G.S.; Park, N.G.; Ko, M.J. Flexible perovskite solar cells. *Joule* **2019**, *3*, 1850–1880. [CrossRef]
10. Xie, F.X.; Su, H.; Mao, J.; Wong, K.S.; Choy, W.C. Evolution of diffusion length and trap state induced by chloride in perovskite solar cell. *J. Phys. Chem. C* **2016**, *120*, 21248–21253. [CrossRef]
11. Park, N.G. Methodologies for high efficiency perovskite solar cells. *Nano Converg.* **2016**, *3*, 15. [CrossRef]
12. Lan, Z.R.; Wang, Y.D.; Shao, J.Y.; Ma, D.X.; Liu, Z.; Li, D.; Hou, Y.; Yao, J.; Zhong, Y.W. Surface Passivation with Diaminopropane Dihydroiodide for p-i-n Perovskite Solar Cells with over 25% Efficiency. *Adv. Funct. Mater.* **2024**, *34*, 2312426. [CrossRef]
13. Elumalai, N.K.; Mahmud, M.A.; Wang, D.; Uddin, A. Perovskite solar cells: Progress and advancements. *Energies* **2016**, *9*, 861. [CrossRef]
14. Bimli, S.; Manjunath, V.; Mulani, S.R.; Miglani, A.; Game, O.S.; Devan, R.S. Theoretical investigations of all inorganic Cs_2SnI_6 double perovskite solar cells for efficiency∼30%. *Sol. Energy* **2023**, *256*, 76–87. [CrossRef]
15. Petrus, M.L.; Schlipf, J.; Li, C.; Gujar, T.P.; Giesbrecht, N.; Müller-Buschbaum, P.; Thelakkat, M.; Bein, T.; Hüttner, S.; Docampo, P. Capturing the sun: A review of the challenges and perspectives of perovskite solar cells. *Adv. Energy Mater.* **2017**, *7*, 1700264. [CrossRef]
16. Ansari, M.I.H.; Qurashi, A.; Nazeeruddin, M.K. Frontiers, opportunities, and challenges in perovskite solar cells: A critical review. *J. Photochem. Photobiol. C* **2018**, *35*, 1–24. [CrossRef]
17. Chung, J.-H.; Song, J.; Im, J.; Androulakis, C.; Malliakas, C.D.; Li, H.; Freeman, A.J.; Kenney, J.T.; Kanatzidis, M.G. $CsSnI_3$: Semiconductor or metal? High electrical conductivity and strong near-infrared photoluminescence from a single material. High hole mobility and phase-transitions. *J. Am. Chem. Soc.* **2012**, *134*, 8579–8587. [CrossRef] [PubMed]
18. Correa-Baena, J.-P.; Saliba, M.; Buonassisi, T.; Grätzel, M.; Abate, A.; Tress, W.; Hagfeldt, A. Promises and challenges of perovskite solar cells. *Science* **2017**, *358*, 739–744. [CrossRef] [PubMed]
19. Goetz, K.P.; Taylor, A.D.; Hofstetter, Y.J.; Vaynzof, Y. Sustainability in perovskite solar cells. *ACS Appl. Mater. Interfaces* **2020**, *13*, 1–17. [CrossRef] [PubMed]
20. Wang, X.; Sarvari, H.; Dang, H.; Singh, V.; Chen, Z. Preparation and evaluation of perovskite solar cells in the absolute atmospheric environment. In *Optoelectronic Devices and Integration VI*; SPIE: Bellingham, WA, USA, 2016; Volume 10019, pp. 37–43.
21. Chen, H.; Xiang, S.; Li, W.; Liu, H.; Zhu, L.; Yang, S. Inorganic perovskite solar cells: A rapidly growing field. *Solar RRL* **2018**, *2*, 1700188. [CrossRef]
22. Zhang, J.; Hodes, G.; Jin, Z.; Liu, S. All-inorganic $CsPbX_3$ perovskite solar cells: Progress and prospects. *Angew. Chem. Int. Ed.* **2019**, *58*, 15596–15618. [CrossRef]
23. Liu, C.; Li, W.; Zhang, C.; Ma, Y.; Fan, J.; Mai, Y. All-inorganic $CsPbI_2Br$ perovskite solar cells with high efficiency exceeding 13%. *J. Am. Chem. Soc.* **2018**, *140*, 3825–3828. [CrossRef] [PubMed]
24. Wang, Z.K.; Li, M.; Yang, Y.G.; Hu, Y.; Ma, H.; Gao, X.Y.; Liao, L.S. High efficiency Pb–In binary metal perovskite solar cells. *Adv. Mater.* **2016**, *28*, 6695–6703. [CrossRef] [PubMed]
25. Flora, G.; Gupta, D.; Tiwari, A. Toxicity of lead: A review with recent updates. *Interdiscip. Toxicol.* **2012**, *5*, 47–58. [CrossRef] [PubMed]
26. Gamal, N.; Sedky, S.H.; Shaker, A.; Fedawy, M. Design of lead-free perovskite solar cell using $Zn_{1-x}Mg_xO$ as ETL: SCAPS device simulation. *Optik* **2021**, *242*, 167306. [CrossRef]
27. Benmessaoud, R.I. *Human and Eco-Toxicological Impacts of Organometallic Halide Perovskites*; EPFL: Lausanne, Switzerland, 2017.
28. Peng, Y.; Liu, Y. Lead–An Obstacle for Installing Perovskite Devices? *Perovskite Mater. Devices* **2022**, *2*, 629–653.
29. Giustino, F.; Snaith, H.J. Toward lead-free perovskite solar cells. *ACS Energy Lett.* **2016**, *1*, 1233–1240. [CrossRef]
30. Cao, J.; Yan, F. Recent progress in tin-based perovskite solar cells. *Energy Environ. Sci.* **2021**, *14*, 1286–1325. [CrossRef]

31. Zhang, H.; Zhang, W.; Lu, Y. Performance simulation of lead-free perovskite solar cells. In Proceedings of the 2022 14th International Conference on Measuring Technology and Mechatronics Automation (ICMTMA), Changsha, China, 15–16 January 2022; IEEE: Piscataway, NJ, USA, 2022; pp. 789–793.
32. Lin, S.; Zhang, B.; Lü, T.Y.; Zheng, J.C.; Pan, H.; Chen, H.; Lin, H.; Li, X.; Zhou, J. Inorganic lead-free B-γ-$CsSnI_3$ perovskite solar cells using diverse electron-transporting materials: A simulation study. *ACS Omega* **2021**, *6*, 26689–26698. [CrossRef] [PubMed]
33. Liu, B.; Long, M.; Cai, M.Q.; Yang, J. Influence of the number of layers on ultrathin $CsSnI_3$ perovskite: From electronic structure to carrier mobility. *J. Phys. D Appl. Phys.* **2018**, *51*, 105101. [CrossRef]
34. Wang, N.; Zhou, Y.; Ju, M.G.; Garces, H.F.; Ding, T.; Pang, S.; Zeng, X.C.; Padture, N.P.; Sun, X.W. Heterojunction-depleted lead-free perovskite solar cells with coarse-grained B-γ-$CsSnI_3$ thin films. *Adv. Energy Mater.* **2016**, *6*, 1601130. [CrossRef]
35. Li, B.; Di, H.; Chang, B.; Yin, R.; Fu, L.; Zhang, Y.N.; Yin, L. Efficient passivation strategy on Sn related defects for high performance all-Inorganic $CsSnI_3$ perovskite solar cells. *Adv. Funct. Mater.* **2021**, *31*, 2007447. [CrossRef]
36. Li, L.; Zhai, T.; Bando, Y.; Golberg, D. Recent progress of one-dimensional ZnO nanostructured solar cells. *Nano Energy* **2012**, *1*, 91–106. [CrossRef]
37. Kumari, N.; Patel, S.R.; Gohel, J.V. Optical and structural properties of ZnO thin films prepared by spray pyrolysis for enhanced efficiency perovskite solar cell application. *Opt. Quantum Electron.* **2018**, *50*, 180. [CrossRef]
38. Michaelson, H.B. The work function of the elements and its periodicity. *J. Appl. Phys.* **1977**, *48*, 4729–4733. [CrossRef]
39. Milnes, A.G. *Heterojunctions and Metal Semiconductor Junctions*; Elsevier: Amsterdam, The Netherlands, 2012.
40. Ma, F.; Zhao, Y.; Li, J.; Zhang, X.; Gu, H.; You, J. Nickel oxide for inverted structure perovskite solar cells. *J. Energy Chem.* **2021**, *52*, 393–411. [CrossRef]
41. Sajid, S.; Elseman, A.M.; Huang, H.; Ji, J.; Dou, S.; Jiang, H.; Liu, X.; Wei, D.; Cui, P.; Li, M. Breakthroughs in NiOx-HTMs towards stable, low-cost and efficient perovskite solar cells. *Nano Energy* **2018**, *51*, 408–424. [CrossRef]
42. Fatima, Q.; Haidry, A.A.; Hussain, R.; Zhang, H. Device simulation of a thin-layer $CsSnI_3$-based solar cell with enhanced 31.09% efficiency. *Energy Fuel* **2023**, *37*, 7411–7423. [CrossRef]
43. Dunfield, S.P.; Bliss, L.; Zhang, F.; Luther, J.M.; Zhu, K.; van Hest, M.F.A.M.; Reese, M.O.; Berry, J.J. From defects to degradation: A mechanistic understanding of degradation in perovskite solar cell devices and modules. *Adv. Energy Mater.* **2020**, *10*, 1904054. [CrossRef]
44. Montecucco, R.; Quadrivi, E.; Po, R.; Grancini, G. All-inorganic cesium-based hybrid perovskites for efficient and stable solar cells and modules. *Adv. Energy Mater.* **2021**, *11*, 2100672. [CrossRef]
45. Li, Z.; Wang, R.; Xue, J.; Xing, X.; Yu, C.; Huang, T.; Chu, J.; Wang, K.-L.; Dong, C.; Wei, Z.; et al. Core–shell ZnO@SnO_2 nanoparticles for efficient inorganic perovskite solar cells. *J. Am. Chem. Soc.* **2019**, *141*, 17610–17616. [CrossRef]
46. Moustafa, M.O.; Alzoubi, T. Numerical simulation of single junction InGaN solar cell by SCAPS. *Key Eng. Mater.* **2019**, *821*, 407–413. [CrossRef]
47. Nykyruy, L.; Yavorskyi, R.; Zapukhlyak, Z.; Wisz, G.; Potera, P. Evaluation of CdS/CdTe thin film solar cells: SCAPS thickness simulation and analysis of optical properties. *Opt. Mater.* **2019**, *92*, 319–329. [CrossRef]
48. Landau, L.D.; Bell, J.S.; Kearsley, M.J.; Pitaevskii, L.P.; Lifshitz, E.M.; Sykes, J.B. *Electrodynamics of Continuous Media*; Elsevier: Amsterdam, The Netherlands, 2013; Volume 8.
49. Hossain, M.K.; Toki, G.I.; Kuddus, A.; Mohammed, M.K.; Pandey, R.; Madan, J.; Bhattarai, S.; Rahman, M.F.; Dwivedi, D.K.; Amami, M.; et al. Optimization of the architecture of lead-free $CsSnCl_3$-perovskite solar cells for enhancement of efficiency: A combination of SCAPS-1D and wxAMPS study. *Mater. Chem. Phys.* **2023**, *308*, 128281. [CrossRef]
50. Roy, P.; Sinha, N.K.; Tiwari, S.; Khare, A. Influence of defect density and layer thickness of absorption layer on the performance of tin based perovskite solar cell. *IOP Conf. Ser. Mater. Sci. Eng.* **2020**, *798*, 012020. [CrossRef]
51. Pindolia, G.; Shinde, S.M.; Jha, P.K. Optimization of an inorganic lead free $RbGeI_3$ based perovskite solar cell by SCAPS-1D simulation. *Sol. Energy* **2022**, *236*, 802–821. [CrossRef]
52. Tang, W.; Liu, T.; Fenwick, O. High thermoelectric performance based on $CsSnI_3$ thin films with improved stability. *J. Mater. Chem. A* **2022**, *10*, 7020–7028. [CrossRef]
53. Ravidas, B.K.; Roy, M.K.; Samajdar, D.P. Investigation of photovoltaic performance of lead-free $CsSnI_3$-based perovskite solar cell with different hole transport layers: First Principle Calculations and SCAPS-1D Analysis. *Sol. Energy* **2023**, *249*, 163–173. [CrossRef]
54. Jiang, M.; Tang, J. Simulated development and optimized performance of narrow-bandgap $CsSnI_3$-based all-inorganic perovskite solar cells. *J. Phys. D Appl. Phys.* **2021**, *54*, 465104. [CrossRef]
55. Ma, F.J.; Liu, H.; Liao, B.; Chen, J.; Du, Z.; Samudra, G.S.; Aberle, A.G.; Hoex, B.; Peters, I.M. Impact of Auger recombination parameterisations on predicting silicon wafer solar cell performance. *J. Comput. Electron.* **2014**, *13*, 647–656. [CrossRef]
56. Chantana, J.; Kawano, Y.; Nishimura, T.; Mavlonov, A.; Shen, Q.; Yoshino, K.; Iikubo, S.; Hayase, S.; Minemoto, T. Impact of Auger recombination on performance limitation of perovskite solar cell. *Sol. Energy* **2021**, *217*, 342–353. [CrossRef]
57. Zyoud, S.H.; Zyoud, A.H.; Ahmed, N.M.; Prasad, A.R.; Khan, S.N.; Abdelkader, A.F.; Shahwan, M. Numerical modeling of high conversion efficiency FTO/ZnO/CdS/CZTS/MO thin film-based solar cells: Using SCAPS-1D software. *Crystals* **2021**, *11*, 1468. [CrossRef]
58. Liang, Y.; Cui, X.; Li, F.; Stampfl, C.; Ringer, S.P.; Huang, J.; Zheng, R. Interstitial Hydrogen Anions: A Cause of p-Type Conductivity in $CsSnI_3$. *J. Phys. Chem. C* **2022**, *126*, 14843–14849. [CrossRef]

59. Kumar, M.H.; Dharani, S.; Leong, W.L.; Boix, P.P.; Prabhakar, R.R.; Baikie, T.; Shi, C.; Ding, H.; Ramesh, R.; Asta, M. Lead-free halide perovskite solar cells with high photocurrents realized through vacancy modulation. *Adv. Mater.* **2014**, *26*, 7122–7127. [CrossRef] [PubMed]
60. Bramantyo, A.; Murakami, K.; Okuya, M.; Udhiarto, A.; Poespawati, N.R. Growth of Zinc Oxide Nanorods with the Thickness of Less than or Equal to 1 μm through Zinc Acetate or Zinc Nitrate for Perovskite Solar Cell Applications. *J. Eng.* **2019**, *2019*, 2793853. [CrossRef]
61. Saleem, M.; Fang, L.; Wakeel, A.; Rashad, M.; Kong, C.Y. Simple preparation and characterization of nano-crystalline zinc oxide thin films by sol-gel method on glass substrate. *Sci. Res. J.* **2012**, *2*, 10–15. [CrossRef]
62. Hasuike, N.; Harada, T.; Kiyohara, T.; Nishio, K.; Kisoda, K.; Harima, H. Low temperature synthesis of ZnO thin films by spin-coating technique. *Phys. Status Solidi A* **2011**, *8*, 506–508. [CrossRef]
63. Tang, K.; Huang, S.; Gu, S.; Zhu, S.; Ye, J.; Xu, Z.; Zheng, Y. The roles of buffer layer thickness on the properties of the ZnO epitaxial films. *Appl. Surf. Sci.* **2016**, *388*, 557–564. [CrossRef]
64. Ke, W.; Fang, G.; Liu, Q.; Xiong, L.; Qin, P.; Tao, H.; Wang, J.; Lei, H.; Li, B.; Wan, J.; et al. Low-temperature solution-processed tin oxide as an alternative electron transporting layer for efficient perovskite solar cells. *J. Am. Chem. Soc.* **2015**, *137*, 6730–6733. [CrossRef] [PubMed]
65. Odari, V.; Musembi, R.; Mwabora, J. Device simulation of Sb_2S_3 solar cells by SCAPS-1D software. *Afr. J. Phys. Sci.* **2019**, *3*, 39–54.
66. Zhang, T.; Zeng, G.; Ye, F.; Zhao, X.; Yang, X. Efficient Non-Fullerene Organic Photovoltaic Modules Incorporating As-Cast and Thickness-Insensitive Photoactive Layers. *Adv. Energy Mater.* **2018**, *8*, 1801387. [CrossRef]
67. Mohammed, M.K.; Abdalhadi, S.M.; Kumar, A.; Doshi, O.P.; Al-Mousoi, A.K.; Hussein, H.T.; Alnayli, R.S.; Madan, J.; Tawfeek, A.M.; Rahman, M.F.; et al. Designing a Novel Hole-Transporting Layer for $FAPbI_3$-Based Perovskite Solar Cells. *Energy Fuels* **2023**, *37*, 19870–19881. [CrossRef]
68. Uddin, M.S.; Al Mashud, M.A.; Toki, G.F.; Pandey, R.; Zulfiqar, M.; Saidani, O.; Chandran, K.; Ouladsmane, M.; Hossain, M.K. Lead-free Ge-based perovskite solar cell incorporating TiO_2 and Cu_2O charge transport layers harnessing over 25% efficiency. *J. Opt.* **2023**, 1–17. [CrossRef]
69. Pindolia, G.; Shinde, S.M.; Jha, P.K. Non-leaded, $KSnI_3$ based perovskite solar cell: A DFT study along with SCAPS simulation. *Mater. Chem.* **2023**, *297*, 127426. [CrossRef]
70. Hossain, M.K.; Toki, G.I.; Alam, I.; Pandey, R.; Samajdar, D.P.; Rahman, M.F.; Islam, M.R.; Rubel, M.H.K.; Bencherif, H.; Madan, J.; et al. Numerical simulation and optimization of a $CsPbI_3$-based perovskite solar cell to enhance the power conversion efficiency. *New J. Sci.* **2023**, *47*, 4801–4817. [CrossRef]
71. Bhattarai, S.; Pandey, R.; Madan, J.; Ansari, M.Z.; Hossain, M.K.; Amami, M.; Ahammad, S.H.; Rashed, A.N.Z. Chlorine-doped perovskite materials for highly efficient perovskite solar cell design offering an efficiency of nearly 29%. *Prog. Photovolt. Res. Appl.* **2024**, *32*, 25–34. [CrossRef]
72. Chen, Z.; Chen, G. The effect of absorber thickness on the planar Sb_2S_3 thin film solar cell: Trade-off between light absorption and charge separation. *Sol. Energy* **2020**, *201*, 323–329. [CrossRef]
73. Kundara, R.; Baghel, S. Device modelling of lead free (CH_3NH_3) $2CuX_4$ based perovskite solar cells using SCAPS simulation. *Opt. Quantum Electron.* **2023**, *55*, 968. [CrossRef]
74. Sunny, A.; Rahman, S.; Khatun, M.; Ahmed, S.R.A. Numerical study of high performance HTL-free $CH_3NH_3SnI_3$-based perovskite solar cell by SCAPS-1D. *AIP Adv.* **2021**, *11*, 065102. [CrossRef]
75. Rahman, M.A. Performance analysis of WSe_2-based bifacial solar cells with different electron transport and hole transport materials by SCAPS-1D. *Heliyon* **2022**, *8*, e09800. [CrossRef]
76. Rajagopal, A.; Yao, K.; Jen, A.K.Y. Toward perovskite solar cell commercialization: A perspective and research roadmap based on interfacial engineering. *Adv. Mater.* **2018**, *30*, e1800455. [CrossRef]
77. Saliba, M.; Matsui, T.; Seo, J.-Y.; Domanski, K.; Correa-Baena, J.-P.; Nazeeruddin, M.K.; Zakeeruddin, S.M.; Tress, W.; Abate, A.; Hagfeldt, A. Cesium-containing triple cation perovskite solar cells: Improved stability, reproducibility and high efficiency. *Energy Environ. Sci.* **2016**, *9*, 1989–1997. [CrossRef] [PubMed]
78. Jan, S.T.; Noman, M. Influence of layer thickness, defect density, doping concentration, interface defects, work function, working temperature and reflecting coating on lead-free perovskite solar cell. *Sol. Energy* **2022**, *237*, 29–43.
79. Talbi, A.; Khaaissa, Y.; Nouneh, K.; Feddi, E.M.; El Haouari, M. Effects of temperature, thickness, electron density and defect density on ZnS based solar cells: SCAPS-1D simulation. *Mater. Today Proc.* **2022**, *66*, 116–121. [CrossRef]
80. Samiee, M.; Konduri, S.; Ganapathy, B.; Kottokkaran, R.; Abbas, H.A.; Kitahara, A.; Joshi, P.; Zhang, L.; Noack, M.; Dalal, V. Defect density and dielectric constant in perovskite solar cells. *Appl. Phys. Lett.* **2014**, *105*, 153502. [CrossRef]
81. Son, H.; Jeong, B.-S. Optimization of the Power Conversion Efficiency of $CsPbI_xBr_{3-x}$-Based Perovskite Photovoltaic Solar Cells Using ZnO and NiO_x as an Inorganic Charge Transport Layer. *Appl. Sci.* **2022**, *12*, 8987. [CrossRef]
82. Khatoon, S.; Chakraborty, V.; Yadav, S.K.; Diwakar, S.; Singh, J.; Singh, R.B. Simulation study of $CsPbI_xBr_{1-x}$ and $MAPbI_3$ heterojunction solar cell using SCAPS-1D. *Sol. Energy* **2023**, *254*, 137–157. [CrossRef]
83. Sumona, F.B.; Kashif, M.; Danladi, E.; Tighezza, A.M.; Al-Mahmud, N.; Toki, G.F.; Pandey, R.; Hossain, M.K. Optimization of Perovskite-$KSnI_3$ Solar Cell by Using Different Hole and Electron Transport Layers: A Numerical SCAPS-1D Simulation. *Energy Fuels* **2023**, *37*, 19207–19219. [CrossRef]

84. Jamal, M.S.; Shahahmadi, S.A.; Wadi, M.A.A.; Chelvanathan, P.; Asim, N.; Misran, H.; Hossain, M.I.; Amin, N.; Sopian, K.; Akhtaruzzaman, M. Effect of defect density and energy level mismatch on the performance of perovskite solar cells by numerical simulation. *Optik* **2019**, *182*, 1204–1210. [CrossRef]
85. Danladi, E.; Egbugha, A.C.; Obasi, R.C.; Tasie, N.N.; Achem, C.U.; Haruna, I.S.; Ezeh, L.O. Defect and doping concentration study with series and shunt resistance influence on graphene modified perovskite solar cell: A numerical investigation in SCAPS-1D framework. *J. Indian Chem. Soc.* **2023**, *100*, 101001. [CrossRef]
86. Houck, D.W.; Siegler, T.D.; Korgel, B.A. Predictive modeling of $CuInSe_2$ nanocrystal photovoltaics: The importance of band alignment and carrier diffusion. *ACS Appl. Energy Mater.* **2019**, *2*, 1494–1504. [CrossRef]
87. Mouhib, H.; Wahmane, Y.A.; Atourki, L.; Elfanaoui, A.; Ihlal, A.; Bouabid, K. Numerical investigation of eco-friendly $MASnI_3$ perovskite-based solar cell: Effect of defect density and hole transport layer. *Model. Simul. Mater. Sci. Eng.* **2022**, *30*, 035011. [CrossRef]
88. Noman, M.; Shahzaib, M.; Jan, S.T.; Shah, S.N.; Khan, A.D. 26.48% efficient and stable $FAPbI_3$ perovskite solar cells employing $SrCu_2O_2$ as hole transport layer. *RSC Adv.* **2023**, *13*, 1892–1905. [CrossRef]
89. Gan, Y.; Bi, X.; Liu, Y.; Qin, B.; Li, Q.; Jiang, Q.; Mo, P. Numerical investigation energy conversion performance of tin-based perovskite solar cells using cell capacitance simulator. *Energies* **2020**, *13*, 5907. [CrossRef]
90. Jayan, K.D.; Sebastian, V. Comprehensive device modelling and performance analysis of $MASnI_3$ based perovskite solar cells with diverse ETM, HTM, and back metal contacts. *Sol. Energy* **2021**, *217*, 40–48. [CrossRef]
91. Wang, B.; Kerr, L.L. Nanostructured TiO_2 and ZnO solar cells using CdS as sensitizer: Stability investigation. In Proceedings of the 2010 35th IEEE Photovoltaic Specialists Conference (PVSC), Honolulu, HI, USA, 20–25 June 2010; pp. 001819–001922.
92. Umar, A.; Tiwari, P.; Srivastava, V.; Lohia, V.; Dwivedi, D.K.; Qasem, H.; Akbar, S.; Algadi, H.; Baskoutas, S. Modeling and Simulation of Tin Sulfide (SnS)-Based Solar Cell Using ZnO as Transparent Conductive Oxide (TCO) and NiO as Hole Transport Layer (HTL). *Micromachines* **2022**, *13*, 2073. [CrossRef] [PubMed]
93. Srivastava, V.; Chauhan, R.; Lohia, P. Highly efficient cesium-based halide perovskite solar cell using SCAPS-1D software: Theoretical study. *J. Opt.* **2023**, *52*, 1218–1225. [CrossRef]
94. Mostefaoui, M.; Mazari, H.; Khelifi, S.; Bouraiou, A.; Dabou, R. Simulation of high efficiency CIGS solar cells with SCAPS-1D software. *Energy Procedia* **2015**, *74*, 736–744. [CrossRef]
95. Kendall, J.D.; Boothroyd, A.R. *A Two-Dimensional Analytical Solution of the Poisson and Current Continuity Equations for the Short-Channel MOSFET*, 2nd ed.; Solid State Electron: Ottawa, ON, Canada, 1990; Volume 33, pp. 531–551.
96. Enebe, G.C. Modeling and Simulation of Nanostructured Copper Oxides Solar Cells for Photovoltaic Application. Master's Thesis, University of Johannesburg, Johannesburg, South Africa, 15 October 2019.
97. Helander, M.G.; Greiner, M.T.; Wang, Z.B.; Tang, W.M.; Lu, Z.H. Work function of fluorine doped tin oxide. *J. Vac. Sci. Technol.* **2011**, *29*, 011019. [CrossRef]
98. Ashraf, M.A.; Alam, I. Numerical simulation of CIGS, CISSe and CZTS-based solar cells with In_2S_3 as buffer layer and Au as back contact using SCAPS 1D. *Eng. Res. Express* **2020**, *2*, 035015. [CrossRef]
99. Ahmmed, S.; Aktar, A.; Rahman, M.F.; Hossain, J.; Ismail, A.B.M. A numerical simulation of high efficiency CdS/CdTe based solar cell using NiO HTL and ZnO TCO. *Optik* **2020**, *223*, 165625. [CrossRef]
100. Seyed-Talebi, S.M.; Mahmoudi, M.; Lee, C.H. A comprehensive study of $CsSnI_3$-based perovskite solar cells with different hole transporting layers and back contacts. *Micromachines* **2023**, *14*, 1562. [CrossRef] [PubMed]
101. Jeon, N.J.; Noh, J.H.; Yang, W.S.; Kim, Y.C.; Ryu, S.; Seo, J.; Seok, S.I. Compositional engineering of perovskite materials for high-performance solar cells. *Nature* **2015**, *517*, 476–480. [CrossRef] [PubMed]
102. Wu, B.; Zhou, Y.; Xing, G.; Xu, Q.; Garces, H.F.; Solanki, A.; Goh, T.W.; Padture, N.P.; Sum, T.C. Long minority-carrier diffusion length and low surface-recombination velocity in inorganic lead-free $CsSnI_3$ perovskite crystal for solar cells. *Adv. Funct. Mater.* **2017**, *27*, 1604818. [CrossRef]
103. Kerara, M.; Naas, A.; Reggab, K. Comparative study on perovskite solar cells using P_ZnO, Al_ZnO and In_ZnO as ETMs by SCAPS-1D. *J. Eng. Exact Sci.* **2024**, *10*, 17387. [CrossRef]
104. Hossain, M.K.; Uddin, M.S.; Toki, G.F.I.; Mohammed, M.K.A.; Pandey, R.; Madan, J.; Rahman, M.F.; Islam, M.R.; Bhattarai, S.; Bencherif, H.; et al. Achieving above 24% efficiency with non-toxic $CsSnI_3$ perovskite solar cells by harnessing the potential of the absorber and charge transport layers. *RSC Adv.* **2023**, *13*, 23514–23537. [CrossRef] [PubMed]
105. Pindolia, G.; Shinde, S.M. Unleaded all-inorganic $KSnI_3$ perovskite solar cell: A computational study. *Optik* **2023**, *295*, 171470. [CrossRef]
106. Quintana, M.; Edvinsson, T.; Hagfeldt, A.; Boschloo, G. Comparison of dye-sensitized ZnO and TiO_2 solar cells: Studies of charge transport and carrier lifetime. *J. Phys. Chem. C* **2007**, *111*, 1035–1041. [CrossRef]
107. Ramelan, A.H.; Wahyuningsih, S.; Munawaroh, H.; Narayan, R. ZnO wide bandgap semiconductors preparation for optoelectronic devices. *IOP Conf. Ser. Mater. Sci. Eng.* **2017**, *176*, 012008. [CrossRef]
108. Yin, W.-J.; Yang, J.-H.; Kang, J.; Yan, Y.; Wei, S.-H. Halide perovskite materials for solar cells: A theoretical review. *J. Mater. Chem. A* **2015**, *3*, 8926–8942. [CrossRef]
109. Lenka, T.R.; Soibam, A.C.; Dey, K.; Maung, T.; Lin, F. Numerical analysis of high-efficiency lead-free perovskite solar cell with NiO as hole transport material and PCBM as electron transport material. *CSI Trans. ICT* **2020**, *8*, 111–116. [CrossRef]

110. Diekmann, J.; Caprioglio, P.; Rothhardt, D.; Arvind, M.; Unold, T.; Kirchartz, T.; Neher, D.; Stolterfoht, M. Pathways towards 30% efficient single-junction perovskite solar cells. *Sol. RRL* **2021**, 2100219. [CrossRef]
111. Widianto, E.; Driyo, C.; Sudarsono, S.; Shobih, S.; Nursam, N.M.; Hanna, M.Y.; Absor, M.A.U.; Triyana, K.; Santoso, I. Unraveling the Performance of All-Inorganic Lead-Free $CsSnI_3$-Based Perovskite Photovoltaic with Graphene Oxide Hole Transport Layer. *Adv. Theory Simul.* **2024**, *7*, 2300610. [CrossRef]